



TITLE:

# Model Order Reduction of Cage Induction Motor With Skewed Rotor Slots Using Multiport Cauer Ladder Network Method

AUTHOR(S):

Takahashi, Yasuhito; Fujiwara, Koji; Sugahara, Kengo; Matsuo, Tetsuji

---

CITATION:

Takahashi, Yasuhito ...[et al]. Model Order Reduction of Cage Induction Motor With Skewed Rotor Slots Using Multiport Cauer Ladder Network Method. IEEE Transactions on Magnetics 2023, 59(5): 8201004.

ISSUE DATE:

2023-05

URL:

<http://hdl.handle.net/2433/285298>

RIGHT:

© 2023 IEEE. Personal use of this material is permitted. Permission from IEEE must be obtained for all other uses, in any current or future media, including reprinting/republishing this material for advertising or promotional purposes, creating new collective works, for resale or redistribution to servers or lists, or reuse of any copyrighted component of this work in other works.; This is not the published version. Please cite only the published version. この論文は出版社版ではありません。引用の際には出版社版をご確認ください。

# Model Order Reduction of Cage Induction Motor with Skewed Rotor Slots Using Multiport Cauer Ladder Network Method

Yasuhito Takahashi<sup>1</sup>, Koji Fujiwara<sup>1</sup>, Kengo Sugahara<sup>2</sup>, and Tetsuji Matsuo<sup>3</sup>

<sup>1</sup>Department of Electrical Engineering, Doshisha University, Kyotanabe 610-0394, Japan

<sup>2</sup>Faculty of Science and Engineering, Kindai University, Osaka 577-8502, Japan

<sup>3</sup>Graduate School of Engineering, Kyoto University, Kyoto 615-8510, Japan

**A method for efficiently deriving a reduced-order model of a cage induction motor (IM) with skewed rotor slots is proposed based on the multiport Cauer ladder network (CLN) method. This paper presents several formulations of the multiport CLN method for the skewed rotor, in which the continuity of the bar currents and the space harmonics included in the air-gap flux density waveform are treated differently. The effectiveness of the developed methods was verified from the viewpoints of computational accuracy and cost through application to a practical cage IM with skewed rotor slots.**

**Index Terms**— Cage induction motor, Cauer ladder network, finite-element method, model order reduction, skewed rotor slots.

## I. INTRODUCTION

IN the design of a control system for an electric motor, it is desirable to use an accurate model that can appropriately represent the influence of nonlinear magnetic properties and slot harmonics on machine performance. To derive an accurate model of a cage induction motor (IM), various model order reduction (MOR) methods have been used and extended to nonlinear problems [1]-[4]. In this study, the multiport Cauer ladder network (CLN) method [5] was adopted as the MOR method for a cage IM. This approach constructs the matrix Cauer circuits for the stator and rotor domains separately, and the circuits are connected based on the boundary conditions for the space harmonics (SHs) included in the air-gap flux density waveform [6]. The dominant SHs can be selected based on time and space harmonic analysis [7], [8]. Furthermore, the nonlinear MOR for cage IMs using the multiport CLN method has been proposed [4]. To date, however, the motor MOR based on the CLN is restricted within a two-dimensional (2D) formulation and cannot handle skewed slots, although they are typically adopted to cage IMs to reduce torque ripples. Therefore, a modeling method for the three-dimensional (3D) skewed structure is essentially needed to further enhance the practicality of the MOR for IMs.

With this background, this study investigated a method for efficiently deriving a reduced-order model of a cage IM with skewed structure. A multislice method (MSM) [9] was adopted to model the skewed rotor. This paper proposes three novel formulations of the multiport CLN method for skewed rotor slots, in which the continuity of the bar currents and SHs included in the air-gap flux density waveform are treated differently. Finally, the effectiveness of the developed methods was verified by the steady-state analysis of a practical cage IM from the viewpoints of computational accuracy and cost.

Manuscript received April 1, 2015; revised May 15, 2015 and June 1, 2015; accepted July 1, 2015. Date of publication July 10, 2015; date of current version July 31, 2015. Corresponding author: Yasuhito Takahashi (e-mail: ytakahashi@mail.doshisha.ac.jp).

Color versions of one or more of the figures in this paper are available online at <http://ieeexplore.ieee.org>.

Digital Object Identifier (inserted by IEEE).

## II. METHOD OF ANALYSIS

### A. Multiport CLN Method for Cage IM

Fig. 1 shows the matrix CLN corresponding to the stator and rotor domains in a cage IM [6], in which the SHs of the air-gap flux densities and phase currents/voltages are considered as the input data of each domain. The multiport CLN method with several stages is applied to the rotor domain to consider the frequency characteristics of the eddy-current fields in the secondary conductor. The number of stages is denoted as  $N$ . Because this study focused on a method for modeling skewed rotor slots in the context of the MOR of cage IMs based on the multiport CLN method, linear magnetic properties are assumed as a first step toward the practical use of the developed approach.

A winding resistance  $R_s$  and the inductance matrices  $L_s$ ,  $L_h$ , and  $L_{sh}$  are considered in the stator domain. Here, the three-by-three matrix  $L_s$  denotes the inductances of the primary windings, the  $M$ -by- $M$  matrix  $L_h$  represents the inductances corresponding to the SHs of the air-gap flux density, the three-by- $M$  matrix  $L_{sh}$  represents the interactions between the primary windings and the SHs, and  $M$  is the number of SHs.

To ensure that the sum of the rotor bar currents per pole pair is always zero strictly by considering the circuit connection of the rotor bars, this study adopted the CLN method based on the  $A$ - $\phi$  formulation [8], [10], where  $A$  is the magnetic vector potential and  $\phi$  is the electric scalar potential. The inductance matrix  $L_{2n-1}$  and resistance matrix  $R_{2n}$  in Fig. 1(b) are determined as follows:

$$C^T M_v C (A_{2n+1} - A_{2n-1}) = M_\sigma E_{2n} R_{2n}, \quad (1)$$

$$L_{2n+1} = A_{2n+1}^T C^T M_v C A_{2n+1}, \quad (2)$$

$$\tilde{E}_{2n+2} - E_{2n} = -A_{2n+1} L_{2n+1}^{-1}, \quad (3)$$

$$G^T M_\sigma G \Psi_{2n+2} = -G^T M_\sigma \tilde{E}_{2n+2}, \quad (4)$$

$$E_{2n+2} = \tilde{E}_{2n+2} + G \Psi_{2n+2}, \quad (5)$$

$$R_{2n+2}^{-1} = E_{2n+2}^T M_\sigma E_{2n+2}, \quad (6)$$

using the initial values of  $A_{-1} = \mathbf{0}$  and  $E_0 = \mathbf{0}$ . Here,  $G$  is the discrete gradient operator,  $C$  is the discrete curl operator [11], the positive integer  $n$  is the stage number, and  $L_{2n-1}$  and  $R_{2n}$  are  $M$ -by- $M$  matrices, respectively. When  $n = 0$ , the right-hand side

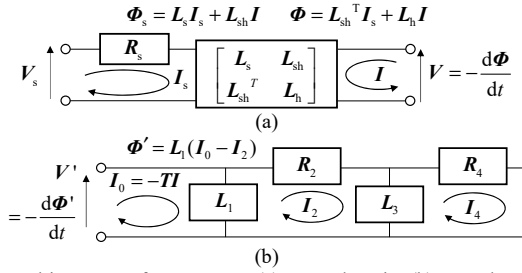


Fig. 1. Multiport CLN for cage IMs: (a) stator domain; (b) rotor domain.

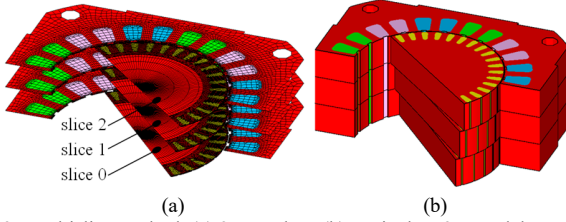


Fig. 2. Multislice method: (a) 2D meshes; (b) equivalent 3D model.

in (1) is replaced with the vectors corresponding to the air-gap magnetic field given by a Neumann boundary condition [6]. The  $(i, j)$ -th entries of  $M_V$  and  $M_\sigma$  are expressed by the magnetic reluctivity, conductivity, and face-element and edge-element basis functions [6]. Matrices  $A_{2n-1}$ ,  $E_{2n}$ , and  $\Psi_{2n}$  consist of the basis vectors associated with the line integrals of the magnetic vector potential and electric field, and the electric scalar potential, respectively.

In Fig. 1(a),  $V$ ,  $I$ , and  $\Phi$  are the vectors comprising the SHs of the circumferential component of the air-gap magnetic field, and the axial components of the air-gap electric field and the air-gap magnetic vector potential, respectively, on the stator-fixed coordinate system; in Fig. 1(b)  $V'$ ,  $I_0$ , and  $\Phi'$  denote those on the rotor-fixed coordinate system. The physical quantities in each domain are connected by  $I_0 = -TI$  and  $\Phi' = T\Phi$ , where the transformation matrix  $T$  is given by [6],[8]

$$T = \text{blockdiag}[T_1, T_2, \dots, T_M], \quad T_m = \begin{bmatrix} \cos m p \omega t & -\sin m p \omega t \\ \sin m p \omega t & \cos m p \omega t \end{bmatrix}. \quad (7)$$

Here,  $\omega$  is the mechanical angular frequency and  $p$  is the number of pole pairs.

### B. Multislice Method

Fig. 2 shows the concept of the MSM, in which the number of slices  $N_s$  is 3. This method is a combination of 2D formulations at several cross-sections of the cage IM, and the positions of the respective rotor meshes change according to the skew angle. Therefore, this method is considered as the stepwise 3D modeling of the rotor, as shown in Fig. 2(b). The bar currents flowing in each bar are kept continuous by imposing equipotential boundary conditions on the interface of the bars. Consequently, the magnetic coupling between the slices is indirectly considered through the bar currents. For the detailed discussion about the accuracy of the MSM compared with a full 3D model of the skewed structure, see, for instance, [12]. In this study, the MSM was used in finite-element analyses (FEAs) of cage IMs with skewed rotor slots, and in the proposed CLN methods described in the next section.

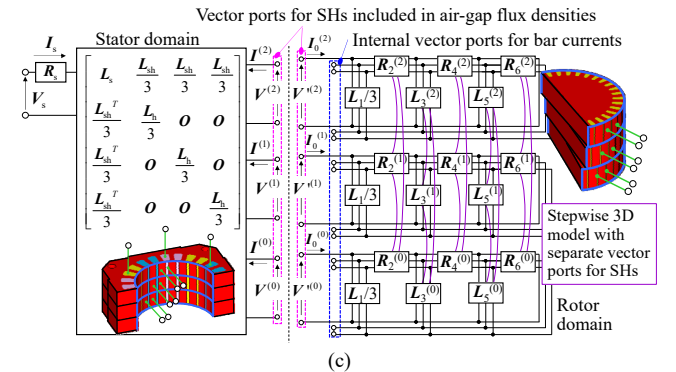
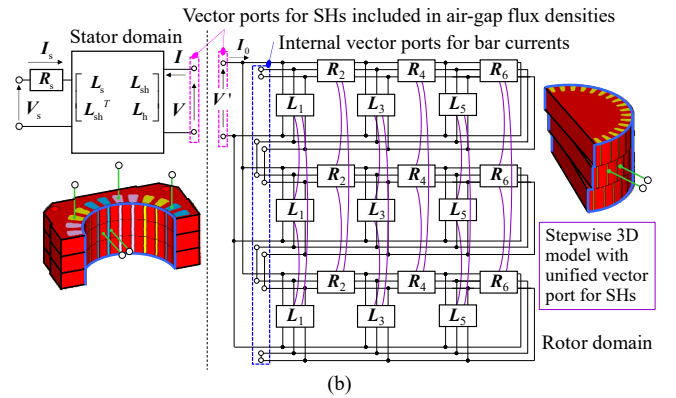
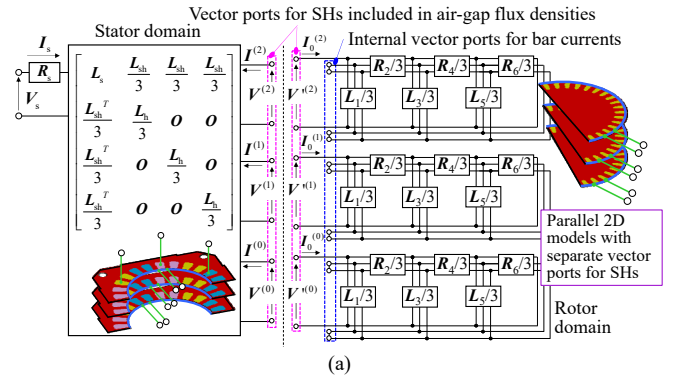


Fig. 3. Equivalent Cauer circuit for cage IM with skewed rotor slots: (a) Method 1; (b) Method 2; (c) Method 3.

### C. Modelling of Skewed Rotor Slots for CLN Method

The simple idea for considering the skewed rotor slots in the multiport CLN method is to connect the several Cauer circuits for the rotor domain in parallel. This is called “Method 1.” Fig. 3(a) shows the equivalent circuit of Method 1 when  $N_s = 3$ . The superscript of  $V$ ,  $I$ ,  $V'$ , and  $I_0$  denotes the slice number. The vector ports for the SHs included in the air-gap flux densities exist independently at each slice. Thus, the sum of the number of SHs at every slice is  $MN_s$ . Here, circuit parameters  $L_h$  and  $L_{sh}$  in the stator domain and  $L_{2n-1}$  and  $R_{2n}$  in the rotor domain are determined by the ordinary CLN method. In Method 1,  $L_h$ ,  $L_{sh}$ ,  $L_{2n-1}$ , and  $R_{2n}$  are divided by  $N_s$  in the equivalent circuit, as shown in Fig. 3(a), because the thickness of each slice is equal to  $1/N_s$  of the axial length of the analyzed cage IM.

The rotor positions of each slice are different owing to the skew angle  $\theta_s$ , although the Cauer circuits for the rotor domain are identical. To consider the difference of the rotor position at respective slices,  $T_m$  in (7) at Slice  $k$  ( $0 \leq k \leq N_s - 1$ ) is given by

$$\mathbf{T}_m^{(k)} = \begin{bmatrix} \cos mp(\omega t - (2k+1-N_s)\theta_s/2N_s) & -\sin mp(\omega t - (2k+1-N_s)\theta_s/2N_s) \\ \sin mp(\omega t - (2k+1-N_s)\theta_s/2N_s) & \cos mp(\omega t - (2k+1-N_s)\theta_s/2N_s) \end{bmatrix}. \quad (8)$$

The bar current is not continuous because the internal vector ports corresponding to bar currents are not connected between the slices in Method 1, which results in inadequate accuracy. The circuit equations for the rotor domain are block diagonal owing to neglecting the magnetic coupling between the slices.

To directly derive the Caer circuit for the rotor domain by considering the skewed structure, the multiport CLN method is applied to the stepwise 3D model derived from the MSM shown in Fig. 2(b). This is called ‘‘Method 2.’’ Fig. 3(b) shows the corresponding equivalent Caer circuit when  $N_s = 3$ . In this approach, the vector ports for the SHs are unified, and the sum of the number of SHs is  $M$  as is the case in the ordinary CLN method. The equivalent circuits for the stator and rotor domains are connected using  $\mathbf{T}$  in (7). Method 2 essentially satisfies the bar current continuity because  $\mathbf{L}_{2n-1}$  and  $\mathbf{R}_{2n}$  in the rotor domain are determined based on the stepwise 3D model, although the computational cost required to derive the circuit parameters increases. However, it is assumed that the amplitudes of the dominant SHs are constant along the axis direction, which may lead to insufficient computational accuracy.

To solve this problem, the SHs included in the air-gap flux densities at each slice are separately treated as other vector ports when applying the multiport CLN method to the stepwise 3D model. This is called ‘‘Method 3,’’ and Fig. 3(c) shows the corresponding equivalent circuit when  $N_s = 3$ . Although only the self-resistance  $\mathbf{R}_{2n}^{(k)}$  and self-inductance matrix  $\mathbf{L}_{2n+1}^{(k)}$  at Slice  $k$  are explicitly shown in Fig. 3(c), the mutual-resistance matrix  $\mathbf{R}_{2n}^{(k)(l)}$  and mutual-inductance matrix  $\mathbf{L}_{2n+1}^{(k)(l)}$ , which represent the interactions between Slice  $k$  and Slice  $l$ , also exist in the equivalent circuit for the rotor domain. The sum of the number of SHs at every slice is  $MN_s$ , and the equivalent circuits for each domain are connected at each slice using  $\mathbf{T}$  in (7). Although the computational cost increases with the increase in the number of SHs, the accuracy can be improved by considering the change of the air-gap flux densities along the axis direction.

### III. NUMERICAL RESULTS

The effectiveness of the proposed methods was verified by analyzing the cage IM with semi-closed rotor slots shown in Fig. 4;  $\theta_s$  is equivalent to 1-rotor slot pitch, and  $N_s$  is 3. The number of time steps per period was set to 360 for all calculations in this paper to evaluate the SHs in the air-gap flux densities accurately. The dominant SHs for the multiport CLN method were determined based on the steady-state solutions at slip  $s = 0$  using the method proposed in [8]. In this case, the number of selected SHs is 36. Initial values for transient calculations of the FEA and CLN methods were determined based on time-harmonic eddy-current analysis [13], in which the slip frequency is applied to the rotor region. The ICCG method was used as a linear iterative solver, and the convergence criterion  $\epsilon$  was set to  $10^{-8}$ . When deriving the circuit parameters using Method 3, the ICMRTR method [14] was used to stabilize the convergence behavior, and  $\epsilon$  was set to  $10^{-7}$ .

Fig. 5 compares the phase current and torque waveforms at  $s$

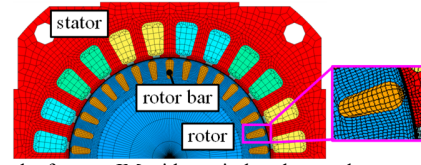


Fig. 4. 2D mesh of a cage IM with semi-closed rotor slots.

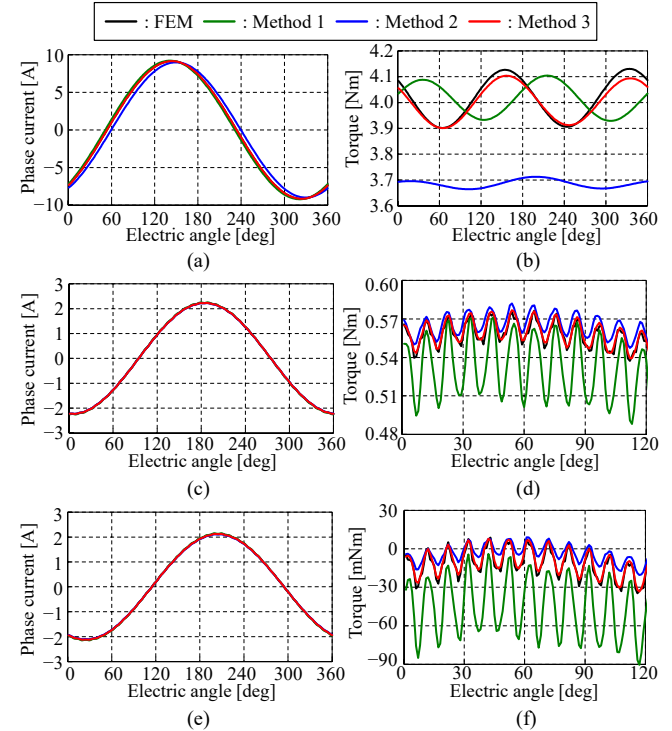


Fig. 5. Numerical results obtained by FEM and CLN methods: (a) phase current at  $s = 1$ ; (b) torque at  $s = 1$ ; (c) phase current at  $s = 0.0588$ ; (d) torque at  $s = 0.0588$ ; (e) phase current at  $s = 0$ ; (f) torque at  $s = 0$ .

$= 1$ ,  $s = 0.0588$ , and  $s = 0$  when applying a sinusoidal voltage waveform with a frequency of 50 Hz and rms value of 100 V. The phase current waveforms obtained by Method 1 are in good agreement with the reference solutions obtained using the FEM. However, the torque waveforms differ substantially at any slip in Method 1, because the continuity of the bar currents is ignored. In Method 2, the phase current waveforms are slightly different, and the torque waveform is entirely different at  $s = 1$ . In contrast, the numerical results are in relatively good agreement with those obtained by the FEM at a small slip. The reason for this is the assumption that the SHs included in the air-gap flux densities are identical along the axis direction.

Fig. 6 shows the distribution of flux density at each slice at respective slips when  $N_s = 3$ . In Fig. 6, the vector diagram of the main flux  $\Phi_m$  and the magnetomotive forces  $F_1'$  and  $F_2$  corresponding to the primary and secondary load currents are also shown. The resultant vector of  $F_1'$  and  $F_2$  strengthens  $\Phi_m$  at Slice 2 because  $F_2$  rotates counterclockwise due to its position skewed to the rotational direction. In contrast, the resultant vector of  $F_1'$  and  $F_2$  weakens  $\Phi_m$  at Slice 0 because  $F_2$  rotates clockwise due to its position skewed to the anti-rotational direction. Consequently, the flux distribution changes drastically at each slice at  $s = 1$ . When  $s$  is large, the effect of the secondary current is significant, which results in the change

of the air-gap flux density along the axis direction. As  $s$  approaches zero, the effect of the secondary current decreases, and the difference in the distribution of the flux densities between the slices is gradually reduced. Therefore, Method 2 can obtain the appropriate numerical results at a small slip.

Method 3 can obtain almost the same numerical results as the FEM at any slip because it can consider the continuity of bar currents and the change of the air-gap flux densities along the axis direction. Although the torque waveform at  $s = 1$  is slightly different from the reference solution, the accuracy can be easily improved by increasing the number of selected SHs.

Table I presents the calculation time required to extract the dominant SHs using the FEM, derive the circuit parameters using the CLN method, and perform transient analysis at  $s = 0.0588$ . The values in parentheses denote the number of periods required to obtain the steady state during a period. The derivation of the circuit parameters using Method 1 is faster compared with Methods 2 and 3 because they can be determined by the ordinary CLN method. The number of SHs in Fig. 3(b) is smaller than those in Figs. 3(a) and 3(c). Thus, the transient analysis based on Method 2 is much faster than other methods. Method 3 requires more calculation time compared with Methods 1 and 2 because the circuit parameters shown in Fig. 3(c) are derived using quasi-3D FEAs based on the MSM and the number of SHs in the equivalent circuit is  $MN_s$ . However, the transient analysis based on Method 3 is approximately 100 times faster compared with the FEM. When using the proposed method, we need the preliminary calculations for extracting dominant SHs and deriving circuit parameters only once. Therefore, it is suitable to situations where transient analyses are repeatedly performed. For instance, the CLN can be effectively used as an accurate motor model in the design of the control system. When the performance of the cage IM is approximated, Method 2 is also effective because it is very fast and has acceptable accuracy at a small slip, which reflects the typical operating condition of practical motors.

#### IV. CONCLUSION

This study developed novel reduced-order models of cage IMs with skewed rotor slots in the context of the CLN method. As a result of applying the proposed approaches to a practical cage IM, the effectiveness of Method 3, in which the SHs of the air-gap flux densities at each slice are separately treated as other vector ports in the equivalent circuit derived from the stepwise 3D model, was confirmed from the viewpoints of computational accuracy and cost. In future work, we will combine the developed method with nonlinear MOR using a parameterized CLN method to apply it to a cage IM with closed rotor slots.

#### ACKNOWLEDGMENT

This study was supported by JSPS KAKENHI (Grant-in-Aid for Scientific Research (C)) Grant Number JP20K04443.

#### REFERENCES

[1] T. Shimotani, Y. Sato, T. Sato, and H. Igarashi, "Fast finite-element analysis of motors using block model order reduction," *IEEE Trans. Magn.*, vol. 52, no. 3, Art. no. 7207004, 2016.

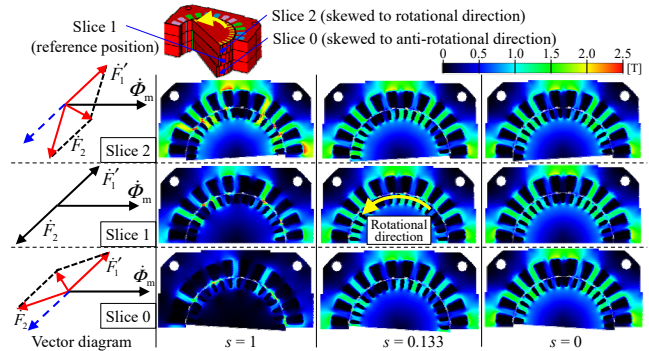


Fig. 6. Comparison of flux density distribution at each slip.

TABLE I  
COMPUTATIONAL TIMES FOR FEM AND CLN METHODS

Method	Extracting dominant SHs	Computational time [s]	
		Deriving circuit parameters	Transient analysis at $s = 0.0588$
Method 1		242.9	18.9 (3)
Method 2	891.4 (2)	574.9	2.7 (3)
Method 3		2056.1	36.0 (3)
FEM	-	-	3672.1 (3)

Intel Xeon Gold 6148 was used.

[2] L. Montier, T. Henneron, S. Clénet, and B. Goursaud, "Model order reduction applied to a linear finite element model of a squirrel cage induction machine based on POD approach," *IEEE Trans. Magn.*, vol. 57, no. 6, Art. no. 8105204, 2021.

[3] M. Nell, F. Müller, and K. Hameyer, "Model order reduction applied to a non-linear finite element model of a squirrel cage induction machine," *IEEE Trans. Magn.*, vol. 57, no. 6, Art. no. 8105204, 2018.

[4] M. Tobita and T. Matsuo, "Nonlinear model order reduction of induction motors using parameterized CLN method," *IEEE Trans. Magn.*, vol. 58, no. 9, Art. no. 8205504, 2022.

[5] A. Kameari, H. Ebrahimi, K. Sugahara, Y. Shindo, and T. Matsuo, "Cauer ladder network representation of eddy-current fields for model order reduction using finite element method," *IEEE Trans. Magn.*, vol. 54, no. 3, Art. no. 7201804, 2018.

[6] T. Matsuo, K. Sugahara, A. Kameari, and Y. Shindo, "Model order reduction of an induction motor using a Cauer ladder network," *IEEE Trans. Magn.*, vol. 56, no. 3, Art. no. 7514704, 2020.

[7] H. Mikami, K. Ide, M. Takahashi, and K. Kajiwara, "Dynamic harmonic field analysis of an inverter-fed induction motor for estimating harmonic secondary current and electromagnetic force," *IEEE Trans. Energy Convers.*, vol. 14, no. 3, pp. 464-470, 1999.

[8] Y. Takahashi, K. Fujiwara, K. Sugahara, and T. Matsuo, "Reduced order modeling based on multiport Cauer ladder network for space harmonics of air-gap flux density in cage induction motor," *IEEE Trans. Magn.*, vol. 58, no. 8, Art. no. 8203306, 2022.

[9] S. L. Ho and W. N. Fu, "A comprehensive approach to the solution of direct-coupled multislice model of skewed rotor induction motors using time-stepping eddy-current finite element method," *IEEE Trans. Magn.*, vol. 33, no. 3, pp. 2265-2273, 1997.

[10] H. Ebrahimi, K. Sugahara, T. Matsuo, H. Kaimori, and A. Kameari, "Modal decomposition of 3-D quasi-static Maxwell equations by cauer ladder network representation," *IEEE Trans. Magn.*, vol. 56, no. 3, Art. no. 7513004, 2020.

[11] A. Bossavit, *Computational Electromagnetism*, New York: Academic, 1998.

[12] K. Yamada, Y. Takahashi, and K. Fujiwara, "Simplified 3-D modeling for skewed rotor slots with end-ring of cage induction motors," *IEEE Trans. Magn.*, vol. 38, no. 2, Art. no. 8101604, 2016.

[13] K. Yamazaki, "An efficient procedure to calculate equivalent circuit parameter of induction motor using 3-D nonlinear time-stepping finite-element method," *IEEE Trans. Magn.*, vol. 38, no. 2, pp. 1281-1284, 2002.

[14] T. Tsuburaya, Y. Okamoto, K. Fujiwara, and S. Sato, "Improvement of the preconditioned MRTR method with Eisenstat's technique in real symmetric sparse matrices," *IEEE Trans. Magn.*, vol. 49, no. 5, pp. 1641-1644, 2013.